

A track length estimator method for dose calculations in low-energy X-ray irradiations: implementation, properties and performance

F. Baldacci¹, A. Mittone^{3,4}, A. Bravin², P. Coan^{3,4}, F. Delaire¹, C. Ferrero², S. Gasilov³, J.M. Létang¹, D. Sarrut¹, F. Smekens¹, N. Freud^{1,*}

¹ Université de Lyon, CREATIS; CNRS UMR5220; Inserm U1044; INSA-Lyon; Université Lyon 1; Centre Léon Bérard, France

² European Synchrotron Radiation Facility, Grenoble, France

³ Department of Physics, LMU Munich, Germany

⁴ Faculty of Medicine, LMU Munich, Germany

Received 20 October 2013; accepted 15 April 2014

Abstract

The track length estimator (TLE) method, an “on-the-fly” fluence tally in Monte Carlo (MC) simulations, recently implemented in GATE 6.2, is known as a powerful tool to accelerate dose calculations in the domain of low-energy X-ray irradiations using the kerma approximation. Overall efficiency gains of the TLE with respect to analogous MC were reported in the literature for regions of interest in various applications (photon beam radiation therapy, X-ray imaging). The behaviour of the TLE method in terms of statistical properties, dose deposition patterns, and computational efficiency compared to analogous MC simulations was investigated. The statistical properties of the dose deposition were first assessed. Derivations of the variance reduction factor of TLE versus analogous MC were carried out, starting from the expression of the dose estimate variance in the TLE and analogous MC schemes. Two test cases were chosen to benchmark the TLE performance in comparison with analogous MC: (i) a small animal irradiation under stereotactic synchrotron radiation therapy conditions and (ii) the irradiation of a human pelvis during a cone beam computed tomography acquisition. Dose distribution patterns and efficiency gain maps were analysed. The efficiency gain exhibits strong variations within

Die Track-Length-Estimator-Methode für Dosisberechnungen bei niederenergetischen Bestrahlungen: Einrichtung, Eigenschaften und Rechenleistung

Zusammenfassung

Die Track-Length-Estimator (TLE)-Methode ist ein rechnerisch sehr effizientes Verfahren für Monte-Carlo (MC)-Simulationen, welches kürzlich in GATE 6.2 implementiert wurde. Sie wird zur Beschleunigung der Dosisberechnungen im Umfeld der niederenergetischen Röntgenstrahlung mit Hilfe der Kerma-Annäherung eingesetzt. Über die Effizienzsteigerung der TLE-Methode im Vergleich mit der analogen MC-Methode wurde in der Literatur in Bezug auf zahlreiche Anwendungen (darunter Strahlentherapie, Röntgenbildgebung) berichtet. Wir haben die TLE-Methode hinsichtlich statistischer Größen, Strahledosisverteilungen und Recheneffizienz im Vergleich mit analogen MC-Simulationen untersucht. Zunächst wurden die statistischen Eigenschaften der abgegebenen Röntgendosis analysiert. Ausgehend vom jeweiligen Ausdruck der mit der Dosisabschätzung verbundenen Varianz bei der TLE- und der analogen MC-Methode, wurde der

* Corresponding author. Dr. Nicolas Freud, CREATIS, INSA, 7 av. Jean Capelle Bât. Blaise Pascal 69621 Villeurbanne cedex, France. Tel.: +33610579001
E-mail: nicolas.freud@insa-lyon.fr (N. Freud).

a given irradiation case, depending on the geometrical (voxel size, ballistics) and physical (material and beam properties) parameters on the voxel scale. Typical values lie between 10 and 10^3 , with lower levels in dense regions (bone) outside the irradiated channels (scattered dose only), and higher levels in soft tissues directly exposed to the beams.

Keywords: Monte Carlo simulation, GATE, Track length estimator, Dose calculation, Kerma approximation, Variance reduction

Varianzreduktionsfaktor der TLE- gegenüber der analogen MC-Methode hergeleitet. Zwei Testfälle wurden zum Vergleich der Leistungsfähigkeiten der TLE- und der analogen MC-Methode untersucht: (i) die Bestrahlung eines Kleintieres bei stereotaktischer Synchrotronstrahlentherapie und (ii) die Bestrahlung eines menschlichen Beckens bei einer Cone-Beam-Computertomographie. Dosisverteilungen und Verteilungen der Effizienzsteigerungsfaktoren wurden analysiert. Letztere zeigen große Unterschiede innerhalb eines gegebenen Bestrahlungsfeldes und zwar in Abhängigkeit der geometrischen (Voxelgröße, Ballistik) und physikalischen (Material- und Strahleigenschaften) Parameter auf der Voxelskala. Typische Werte liegen zwischen 10 und 10^3 , wobei niedrigere Werte in dichten Materialien (Knochen) außerhalb der bestrahlten Bereiche (nur Streudosis) und höhere Werte in weichen, direkt im Strahlenfeld liegenden Geweben festzustellen sind.

Schlüsselwörter: Monte-Carlo-Simulationen, GATE, Track-Length-Estimator, Dosisberechnung, Kerma-Annäherung, Varianzreduktion

1 Introduction

The TLE method is standard of practice in low-energy photon voxel-based dose computation in the kerma approximation [1–5]. The efficiency improvement it provides with respect to analogous MC simulation is well known. However, the statistical properties of the TLE and the parameters influencing its behaviour are still insufficiently documented.

The aim of the present investigation is to bridge this gap, in particular to get an insight into the relative efficiency of the TLE method with respect to analogous MC simulation, through a theoretical derivation and detailed analysis of clinically-realistic test cases. We will focus on two application examples, namely cone beam computed tomography (CBCT) and stereotactic synchrotron radiation therapy (SSRT) [6,7].

The present layout is outlined as follows: the TLE method is briefly summarized (Sec. 2.1) and its implementation in GATE is presented (Sec. 2.2). The statistical properties of the dose deposition in both TLE and analogous MC as well as the variance reduction factor (VRF) are first investigated analytically (Sec. 2.3) and test cases are described (Sec. 2.4). The properties and performance of the TLE are studied in terms of dose distribution patterns (Sec. 3.1), computation time and related statistical uncertainties (Sec. 3.2), distributions of energy deposits (Sec. 3.3), as well as variance reduction factors and efficiency gains (Sec. 3.4).

2 Materials and Methods

2.1 The track length estimator (TLE) method

The TLE technique has long been known as an efficient tool for calculating particle fluences, kerma and absorbed dose [8,9]. It is implemented in various MC codes, such as MCNPX [1,5], and in some tools dedicated to external radiotherapy [3] and brachytherapy [2,4]. For a photon traversing a voxel of volume V , an estimate of the fluence is given by [1,9]:

$$\Phi = \frac{L}{V}, \quad (1)$$

where L is the track length, i.e. the straight-line distance travelled in the voxel between successive collisions. Considering photons with energy E , an estimate of the absorbed dose in charged particle equilibrium is given by [8,10]:

$$D = \Phi E \frac{\mu_{en}}{\rho}, \quad (2)$$

where Φ is the particle fluence and μ_{en}/ρ is the mass energy-absorption coefficient. With the TLE scoring method, a photon deposits energy in all voxels it encounters between successive interaction points (this energy represents the expected value of the deposits that would be observed if a large number of identical photons were transported along the same track),

instead of doing so at interaction points as is the case in analogous MC simulation. This provides a drastic variance reduction.

Local energy deposition by secondary electrons. In the proposed method, secondary electrons are not tracked and their energy is deposited locally. This approximation is satisfactory if:

1. The electron range is smaller than the spatial resolution required. This is generally the case in kV imaging, brachytherapy or other low-energy radiotherapy modalities, e.g. the range of 100 keV electrons in soft tissue is about 0.14 mm [11].
2. There is no significant radiative energy escape (*bremsstrahlung*, atomic de-excitation following electron impact ionization). This assumption is satisfied when the energy-transfer and energy-absorption coefficients present no significant differences. This is the case in the present study, as discussed in the next paragraph.

Generation of the energy-absorption tables. In the keV X-ray domain, the linear energy-absorption (μ_{en}) and energy-transfer (μ_{tr}) coefficients can be considered to be the same quantity [10,12,13]. For tissues composed of elements with atomic numbers $Z \leq 20$, the relative difference between μ_{tr} and μ_{en} remains below 1 % for energy values up to 1 MeV [12]. In the case of a mixture of elements, the mass energy-transfer coefficient ($\frac{\mu_{\text{tr}}}{\rho}$) satisfies the additivity rule. The mass energy-transfer coefficient and hence the mass energy-absorption coefficient of every element with atomic number $1 \leq Z \leq 100$ can be calculated using the EPDL97 database [10,14].

2.2 Implementation of the TLE in GATE

A database of μ_{en} coefficients was generated using EPDL97 for each element with atomic number $1 \leq Z \leq 100$ in the energy range [1 keV, 1 MeV]. This database is loaded during the initialization of the simulation. For each value of Z , the coefficients are tabulated for a set \mathcal{E}_Z of energy values, where the number of values typically ranges from card(\mathcal{E}_1) = 117 to card(\mathcal{E}_{100}) = 868, where card(\mathcal{E}_Z) represents the number of elements of the set \mathcal{E}_Z . Discontinuities are represented by two identical energy values with different μ_{en} values.

During the simulation, the μ_{en} values of a given material are generated and stored the first time this material is encountered. The μ_{en} table of a material M , defined by a mixture of n elements with mass fractions ($\omega_1, \dots, \omega_n$), is computed in two steps: (i) a list of common energy values is determined as $\mathcal{E}_M = \bigcup_{i=1}^n \mathcal{E}_{Z_i}$; (ii) for each energy $E \in \mathcal{E}_M$ and each element of atomic number Z_i in material M , $\mu_{\text{en}}(E, Z_i)$ is computed either by using the value from the initial database if $E \in \mathcal{E}_{Z_i}$ or using a logarithmic interpolation between the μ_{en} values corresponding

to the two nearest energies. Finally, the additivity rule is invoked to obtain the final value of $\mu_{\text{en}}(E, M)$. Once generated and stored in memory, the μ_{en} table of material M is used on-the-fly for determining (possibly with interpolation) the μ_{en} value at the energy of the photon being considered.

The proposed method has been implemented in GATE, an open-source Geant4 application specialised for nuclear medicine imaging and radiotherapy [15]. From the user point of view, an additional *TLEDoseActor* command similar to the conventional *DoseActor* is available [16]. The actor is attached to a volume of interest and creates distribution maps of the deposited energy inside this volume, together with the related statistical uncertainties. With the *TLEDoseActor*, at each photon step in the volume, an amount of energy is deposited according to Eq. 1 and 2.

The volume must be a matrix of voxels defined with *NestedParametrizedVolume*. The size of the voxels must be the same as the size of the dosels. One dosel corresponds to one element of the scoring matrix of the dose distribution.

This new actor is fully compatible with any simulation integrating other actors, even those attached to the same volume. Additionally, it does not alter the results of the other parts of the simulation and does not need electrons to be generated and tracked. It is thus recommended, in order to speed up the computation, to disable their generation if they are not needed by any other element of the simulation. The *TLEDoseActor* and the database of μ_{en} are available in release 6.2 of GATE.

The TLE approach has already been proven rigorously equivalent to the analogous MC simulation of kerma [8,9]. Our TLE implementation was validated against analogous MC simulation as well as experimentally with synchrotron radiation [17]. This validation work will not be discussed any further in this article.

2.3 Statistical analysis of the dose deposition

2.3.1 Estimation of the statistical uncertainty

In MC-based calculations, the dose D deposited in a given voxel per primary particle (or history) is a random variable whose expected value $\langle D \rangle$ is estimated by the arithmetic mean \bar{D}_n of a sample of n simulated primary particles of the population as follows:

$$\langle D \rangle \approx \bar{D}_n = \frac{1}{n} \sum_{i=1}^n d_i, \quad (3)$$

where d_i denotes the value of the dose deposited by history i in the considered voxel. An unbiased estimator of the variance of D is given by [18]

$$s_{n-1}^2[D] = \frac{1}{n-1} \sum_{i=1}^n (d_i - \bar{D}_n)^2 \approx \text{Var}[D] = \sigma^2[D]. \quad (4)$$

The variance of the estimator \bar{D}_n of the expected value of D is

$$\sigma^2 [\bar{D}_n] = \frac{\sigma^2 [D]}{n}. \quad (5)$$

Equation 5 can be rewritten using Eq. 4 as follows [19,20]:

$$\sigma^2 [\bar{D}_n] \approx \frac{s_{n-1}^2 [D]}{n} = \frac{1}{n-1} \left(\frac{1}{n} \sum_{i=1}^n d_i^2 - \left(\frac{1}{n} \sum_{i=1}^n d_i \right)^2 \right). \quad (6)$$

2.3.2 Relative efficiency

The relative efficiency $\epsilon_{\text{TLE}/\text{analog}}$ of the TLE Monte Carlo method with respect to the analogous one is assessed as follows [2,21]:

$$\epsilon_{\text{TLE}/\text{analog}} = \frac{\langle t_{\text{analog}} \rangle \sigma^2 [\bar{D}_{n, \text{analog}}]}{\langle t_{\text{TLE}} \rangle \sigma^2 [\bar{D}_{n, \text{TLE}}]} \quad (7)$$

where $\langle t_{\text{analog}} \rangle$ and $\langle t_{\text{TLE}} \rangle$ are the expected values of the computation time per primary particle for the TLE and analogous MC methods respectively. Most of the computation time for simulating dose distributions by MC is usually spent (i) to track the particles (geometrical and physical processes) and (ii) to score the dose in voxels (memory accesses), as highlighted e.g. for MCNP5 [2]. For a given test case, the particle-tracking time is linear with n (number of histories) and with $1/L$ (the finer the spatial sampling, the longer the simulation), whereas the dose-scoring time is linear with the number of non-zero dose deposits. The first part of equation 7 – the computation time ratio – is specific to the algorithm implementation and software architecture, whereas the second part – the VRF – is an intrinsic characteristic of the method and is detailed in the following section. The TLE method relies on the same MC engine as the analogous – with the additional calculation of μ_{en} plus a few arithmetical operations at each photon step in the volume (see Eq. 2) – but involves more non-zero dose deposits. We will see in Sec. 3.2 that the extra calculation cost in the TLE method is very limited.

2.3.3 An insight into the variance reduction factor

Variance of dose deposit schemes. The application of Eq. 5 to the analogous and TLE MC schemes with the same number of histories in the sample ($n_{\text{analog}} = n_{\text{TLE}}$) leads to:

$$\frac{\sigma^2 [\bar{D}_{n, \text{analog}}]}{\sigma^2 [\bar{D}_{n, \text{TLE}}]} = \frac{\sigma^2 [D_{\text{analog}}]}{\sigma^2 [D_{\text{TLE}}]}. \quad (8)$$

The origin of the VRF is therefore directly linked up with the variance of D , i.e. with the variations of the history-by-history dose deposits d_i . As to the TLE, the variance is reduced by the fact that there are more deposits of lower values. As regards analogous MC, the variance is increased by relatively rare but very high dose deposits due to photoelectric effect. Note that all histories with $d_i = 0$ have to be taken into account to work out the variance values.

Non-zero dose deposits. If we consider only the histories with non-zero dose deposits (denoted with the superscript *), we have the following relations:

$$\langle D \rangle = p^* \langle D^* \rangle \quad \text{and} \quad \langle D^2 \rangle = p^* \langle D^{*2} \rangle \quad (9)$$

where p^* denotes the probability to have a non-zero dose deposit in the population of outcomes of D . Using the standard definition of the variance, it follows that

$$\sigma^2 [D] = p^* \left(\sigma^2 [D^*] + (1 - p^*) \langle D^* \rangle^2 \right). \quad (10)$$

This translates to a new expression for estimating the variance of \bar{D}_n from Eq. 5:

$$s_{n-1}^2 [\bar{D}_n] \approx \frac{n^*}{n^2} \left(s_{n-1}^2 [D^*] + \left(1 - \frac{n^*}{n} \right) \bar{D}_n^{*2} \right) \quad (11)$$

where the probability of non-zero dose deposit is estimated via the ratio n^*/n over the sample of n histories. For dose calculations in large volumes like in CBCT imaging, the numbers of non-zero energy deposits n_{analog}^* and n_{TLE}^* are very small w.r.t. the total numbers of photons, n_{analog} and n_{TLE} , respectively. Therefore, we obtain for the analogous and TLE MC schemes with identical history numbers ($n_{\text{analog}} = n_{\text{TLE}}$):

$$\frac{s_{n-1}^2 [\bar{D}_{n, \text{analog}}]}{s_{n-1}^2 [\bar{D}_{n, \text{TLE}}]} \approx \frac{n_{\text{analog}}^*}{n_{\text{TLE}}^*} \frac{s_{n-1}^2 [D_{\text{analog}}^*] + \bar{D}_{n, \text{analog}}^{*2}}{s_{n-1}^2 [D_{\text{TLE}}^*] + \bar{D}_{n, \text{TLE}}^{*2}}. \quad (12)$$

In addition, the standard deviation and mean value of non-zero individual dose deposits have the same order of magnitude (see examples presented in Fig. 5 and Table 1). A rough approximation of the VRF is therefore given by:

$$\frac{s_{n-1}^2 [\bar{D}_{n, \text{analog}}]}{s_{n-1}^2 [\bar{D}_{n, \text{TLE}}]} \approx \frac{\bar{D}_{n, \text{analog}}^*}{\bar{D}_{n, \text{TLE}}^*} = \frac{n_{\text{TLE}}^*}{n_{\text{analog}}^*}. \quad (13)$$

Analytical expression for a priori variance reduction factor calculations. To derive analytical expressions, all photons are first assumed to have the same energy E_{incident} . This means that the following expressions of the variances are only valid for characterizing the statistical distribution of the primary

Table 1

Characteristics of the dose deposits in two voxels of the pelvis test case, in analogous MC and TLE simulations: the notations are the same as in Eq. 12, the * superscript referring to non-zero dose deposits. The VRF given by Eq. 12 is reported in the last column.

		n^*	$s_{n-1}^2 [D^*]$ (nGy ²)	$\overline{D_n^{*2}}$ (nGy ²)	VRF
Bladder	analogous MC	744	3.170×10^{-1}	1.701×10^{-1}	120.5
	TLE	40175	2.465×10^{-5}	5.021×10^{-5}	
Bone	analogous MC	1174	2.006	3.269	22.0
	TLE	24513	4.683×10^{-3}	6.807×10^{-3}	

energy deposition of monochromatic beams. Equation 10 can be rewritten as:

$$\sigma^2 [D] = p^* \left(\langle D^{*2} \rangle - p^* \langle D^* \rangle^2 \right). \quad (14)$$

In the analogous MC scheme, only photoelectric effect and Compton scattering induce energy deposition. The probability of non-zero dose deposit is therefore:

$$p_{\text{analog}}^* = (1 - \exp(-\mu_{Co, Pe} L)); \quad \mu_{Co, Pe} = \mu_{Co} + \mu_{Pe}, \quad (15)$$

where μ_{Co} and μ_{Pe} are the linear attenuation coefficients for Compton scattering and photoelectric effect, respectively, and L is the traversed distance in a voxel.

Assuming that the mean free paths of the photon processes are much larger than L , a first-order series expansion of the Beer-Lambert attenuation law gives:

$$p_{\text{analog}}^* \approx \mu_{Co, Pe} \langle L \rangle, \quad (16)$$

with $\langle L \rangle$ the expected value of L . The expected values of D^* and D^{*2} in the analogous MC scheme are:

$$\langle D_{\text{analog}}^* \rangle = \frac{\langle E_{\text{analog}}^* \rangle}{\rho V} = \frac{\mu_{Co} \langle E_{Co} \rangle + \mu_{Pe} \langle E_{Pe} \rangle}{\rho V (\mu_{Co} + \mu_{Pe})} \quad (17)$$

and

$$\langle D_{\text{analog}}^{*2} \rangle = \frac{\langle E_{\text{analog}}^{*2} \rangle}{\rho^2 V^2} = \frac{\mu_{Co} \langle E_{Co}^2 \rangle + \mu_{Pe} \langle E_{Pe}^2 \rangle}{\rho^2 V^2 (\mu_{Co} + \mu_{Pe})}, \quad (18)$$

where $\langle E_{Co} \rangle$ is the average energy transferred to the recoil electron during Compton scattering (i.e. binding + kinetic energy), $\langle E_{Pe} \rangle$ is the average total energy transferred to secondary photoelectrons (i.e. the incident energy minus the average energy of the secondary photons). From Eqs 5 and 14 to 18 we obtain the analytical expression of the variance of the analogous MC mean dose estimator:

$$\begin{aligned} \sigma^2 [\overline{D}_{n, \text{analog}}] \\ \approx \frac{\mu_{Co, Pe} \langle L \rangle}{n \rho^2 V^2} \left(\langle E_{\text{analog}}^{*2} \rangle - \mu_{Co, Pe} \langle L \rangle \langle E_{\text{analog}}^* \rangle^2 \right). \end{aligned} \quad (19)$$

In the TLE scheme, all particles falling into the voxel deposit some energy, yielding

$$\sigma^2 [\overline{D}_{n, \text{TLE}}] = \frac{\sigma^2 [L]}{n} \left(\frac{\mu_{\text{en}} E_{\text{incident}}}{\rho V} \right)^2, \quad (20)$$

where $\sigma^2 [L]$ is the variance of the traversed distance in the voxel.

The ratio of the two mean-dose estimator variances for a given number of histories is thus:

$$\begin{aligned} \frac{\sigma^2 [\overline{D}_{n, \text{analog}}]}{\sigma^2 [\overline{D}_{n, \text{TLE}}]} \\ \approx \frac{\mu_{Co, Pe} \langle L \rangle \left(\langle E_{\text{analog}}^{*2} \rangle - \mu_{Co, Pe} \langle L \rangle \langle E_{\text{analog}}^* \rangle^2 \right)}{\sigma^2 [L] \mu_{\text{en}}^2 E_{\text{incident}}^2}. \end{aligned} \quad (21)$$

Note that Eq. 21 also gives the ratio of numbers of histories $n_{\text{analog}}/n_{\text{TLE}}$ that would be required to obtain the same uncertainty on the dose estimate.

The generalization of Eq. 21 – that applies only to primary energy deposition of monochromatic beams – is straightforward. In order to take into account the polychromaticity of the incident beam and the scattered radiation, the numerator and denominator of Eq. 21 should be summed over a spectrum of E_{incident} values, i.e. the energy range of all incident photons which hit the voxel under study, for both primary and secondary radiation. Parameters L , μ_{Pe} , μ_{Co} , E_{Pe} , E_{Co} and μ_{en} vary manifestly with E_{incident} .

2.4 Simulation test cases

The simulations were carried out using Geant4 9.4 with the Penelope physics models. An electron production cut value of 100 keV was used in order to avoid tracking any secondary electron. The cutoff value for the production of

secondary photons was set to $100\ \mu\text{m}$ (the effective cut expressed in energy depends on the material and is typically within 250 eV to 1.5 keV). Two different configurations were simulated:

- An SSRT test case, consisting of a rat head irradiated by ten 50 keV monochromatic parallel beams incident on a target volume loaded with an iodinated agent [7]. The rat head model was obtained by segmenting a CT volume ($85 \times 93 \times 11$ voxels of $0.35 \times 0.35 \times 1.0\ \text{mm}^3$) into four regions: air, water, skull bone (ICRU 46) and a water–iodine mixture with a very large concentration gradient ranging from 0.5 to $32\ \text{mg}\cdot\text{ml}^{-1}$ (Fig. 1(a)). The irradiation was carried out with a fan beam, with a thickness equal to the one of a CT slice and with a width matching the tumour extent. Ten coplanar irradiation ports were used, uniformly distributed over 2π . The rat head was then translated step by step in a direction perpendicular to the fan beam plane for the tumour volume to be completely irradiated. In the present work we considered only the dose deposited by the ten ports which irradiate the sixth slice of the CT volume, where the tumour region is the largest. The dose calculation remains three-dimensional, due to the non-negligible influence of scattering and fluorescence processes.
- A CBCT test case, consisting of a pelvis CT image ($512 \times 512 \times 173$ voxels of $0.908 \times 0.908 \times 3\ \text{mm}^3$, see Fig. 1(b) and 1(c)) irradiated by an X-ray tube, modeled as a point source. The beam spectrum was obtained using the Boone algorithm [22], with 130 kVp and 7 mm Al filtration. The beam was collimated to fully irradiate the flat panel detector and the acquisition consisted of 360 projections (every degree). The flat panel dimensions are $409.6 \times 409.6\ \text{mm}^2$. The distance from the focal spot to the patient axis was 100 cm, and from the patient axis to the flat panel 53.6 cm. A *medium field of view* protocol was used, with the flat panel offset in such a way that the distance between the patient axis and the normal to the flat panel (through its center) was 115 mm. In this protocol, only

slightly more than half of the volume to be reconstructed is irradiated for any given projection.

For each voxel, the tissue composition was set either using a stoichiometric calibration [23] (CBCT pelvis test case), or manually after a volume segmentation process (SSRT rat head test case).

3 Properties and performance of the TLE method

3.1 Dose distribution patterns

Simulations were carried out with the SSRT and CBCT test cases described in Sec. 2.4, with different numbers of histories. The results are presented in Fig. 2 and 3. In the SSRT case, due to the small size of the rat head, the dose is mainly deposited by primary radiation [13]. Two slices away from the direct beams, i.e. in the penumbra, the dose due to scattering (scattered dose) can also be observed. In the CBCT case, the dose distribution reflects the irradiation geometry (full circle *medium field of view* protocol), which results in an axial dissymmetry and a higher level of scattered dose. Both test cases illustrate the typical dose patterns of the analogous MC and TLE methods:

- in an analogous MC simulation, the energy is deposited at the interaction points only, which results in a pepper-like noise and a very slow convergence, thus requiring very high statistics countings;
- with the TLE method, photons deposit their energy in a continuous manner all along their trajectory, instead of doing so at discrete interaction points (see in particular Fig. 2(j) and 3(d)), a fact that substantially reduces the variance (see Sec. 3.2 and 3.4) [13,24].

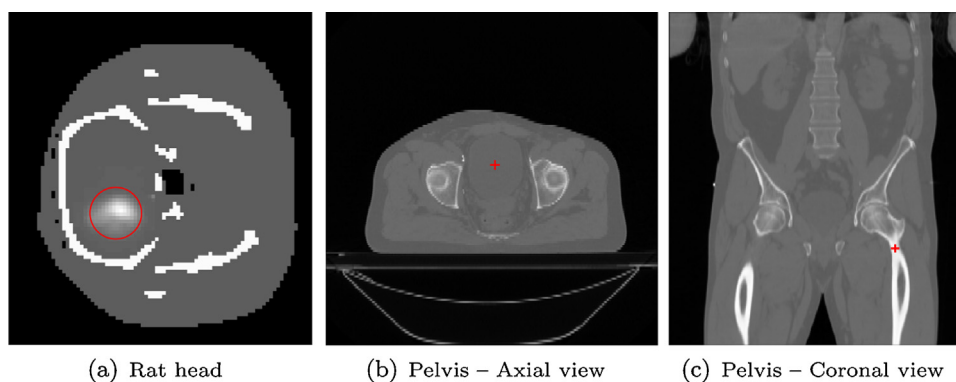


Figure 1. CT models used in the simulation test cases. (a) Sixth slice of a rat head CT scan segmented into four material regions: air, water, cranium bone (ICRU 46) and water–iodine mixture. The red circle indicates the region of interest (ROI) used in Sec. 3.2. (b) and (c) CT scan data from a human pelvis used for the CBCT simulation test case. The red crosses show the voxels of interest (see Sec. 3.3).

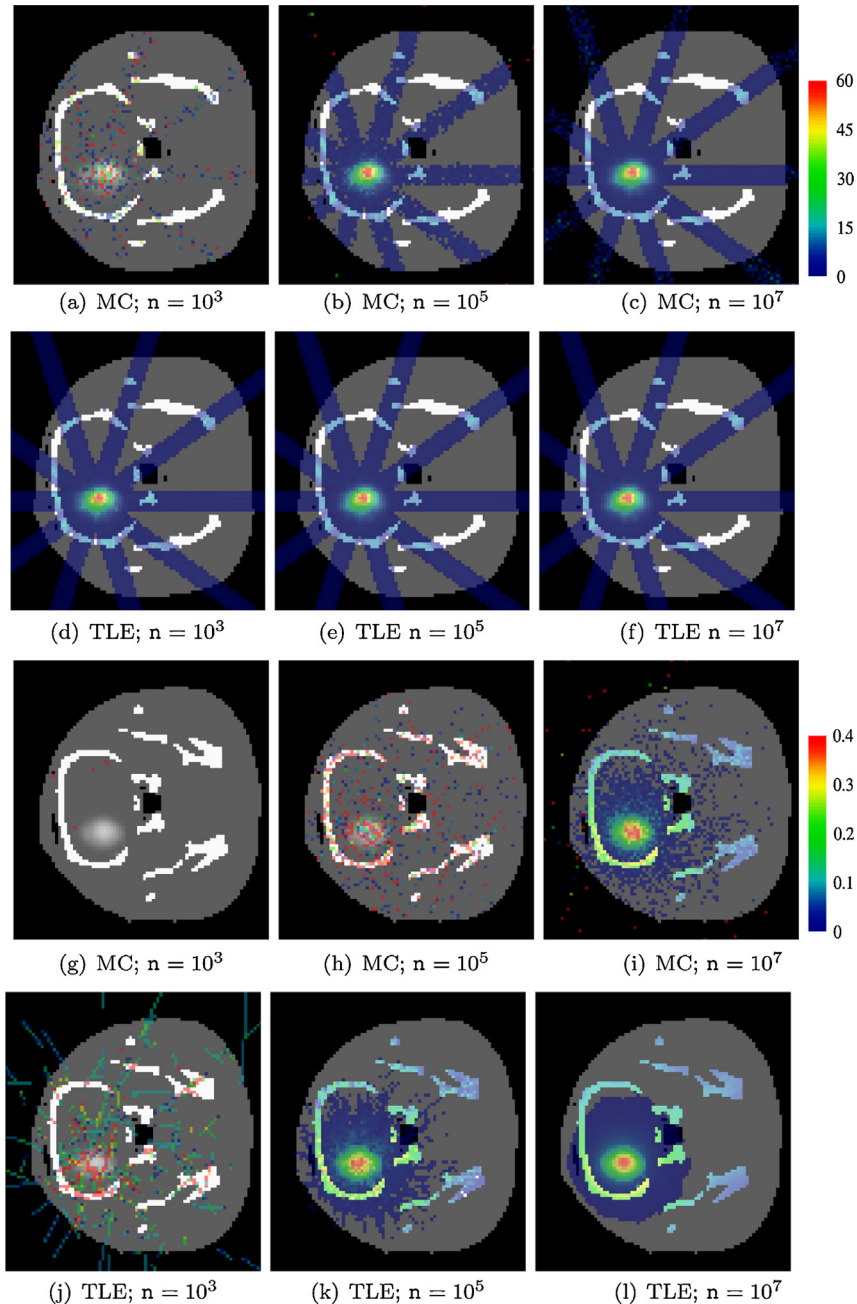


Figure 2. Dose maps of the irradiated rat head slice (two first rows) and two slices away (two bottom rows) in the SSRT test case: comparison between analogous MC and TLE simulations, with different numbers of primary particles. Colour bar values are expressed in pGy per incident photon. Note that the lookup tables used for display were adjusted independently for the two slices.

3.2 Computation time and statistical uncertainties

The computation times required by the TLE and analogous MC methods were first compared. As expected, we observed that the mean computation time was proportional to the number of incident photons traced. In the two test cases, as compared to analogous MC simulation, the TLE method required about 12 % (SSRT test case) or 25% (CBCT test

case) more time to compute the 3D dose distribution with the same number of photons. This is due to the necessary extra calculations and dose scoring. Note that these figures, obtained without electron tracking, depend on the physical settings used in the MC simulation and on the characteristics of the CT model. For example, if the electron processes were activated, the relative cost of the TLE calculations would be even smaller. As an example, the simulation of 10^6 histories

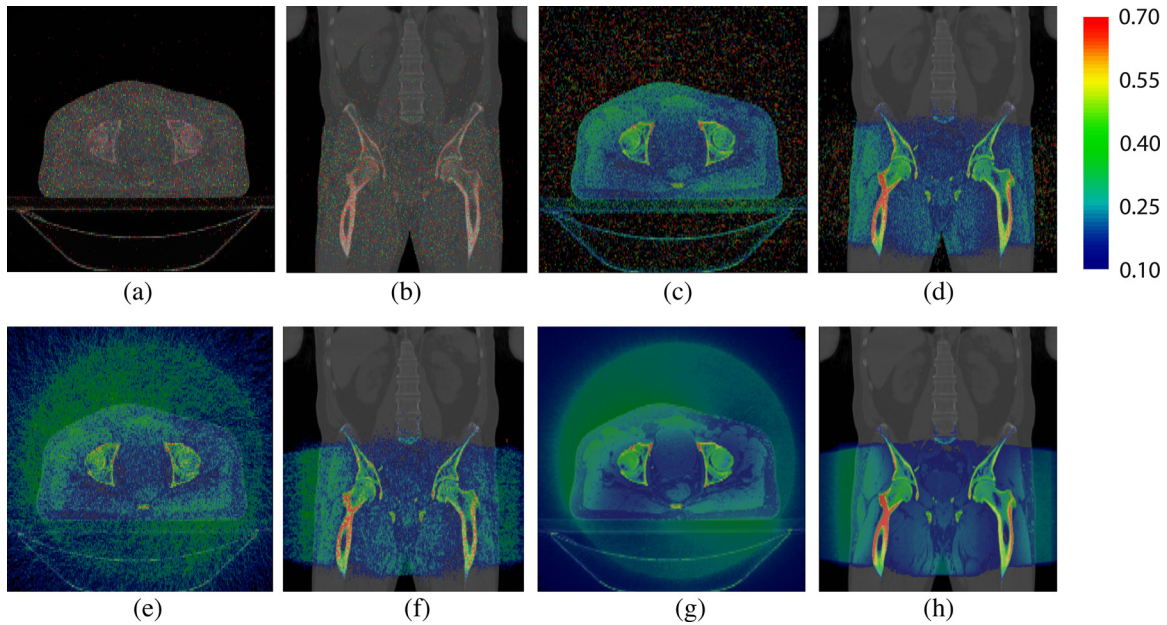


Figure 3. Comparison between the results of the analogous MC (first row) and the TLE (second row) methods for 10^6 (first and second columns) and 10^8 (third and last columns) primary photons. Colour bar values are expressed in fGy per incident photon.

in the CBCT test case took about 21 min (analogous) and 27 min (TLE) on a single core Intel Xeon CPU E5-1660 3.3 GHz.

The VRF reflects the intrinsic behaviour of the two methods, whereas the efficiency also takes into account specific hardware issues. With our implementation, the ratio of the VRF to the efficiency gain is only 1.12 (SSRT test case) or 1.25 (CBCT test case), which is not very significant. In all subsequent sections, the VRF will be used as a figure of merit of TLE vs analogous MC. In order to analyse the statistical behaviour of the TLE method compared to an analogous MC simulation, we first determined the statistical uncertainty in a ROI of the SSRT rat head test case (177 voxels indicated by the red circle in Fig. 1(a)) as a function of the number of incident photons for both computational methods. The statistical uncertainty was computed using Eq. 6 and, in the TLE case, was cross-checked using a batch method [19]. The results (Fig. 4) show that for the same uncertainty the TLE method requires about 240 times less histories than analogous MC simulation. If we consider the same ROI translated by two slices away from the plane of irradiation, the variance reduction (equal to the gain in number of histories) is 140.

As expected from Eq. 6, a horizontal asymptote is observed corresponding to a relative uncertainty equal to unity and the slope of the linear part of the curves is equal to $-1/2$ in log–log scale.

3.3 Analysis of the distribution of energy deposits

In order to investigate the role played by the different terms in Eq. 12, we determined their values for the two voxels indicated by red crosses in Fig. 1(b) and 1(c), corresponding to the

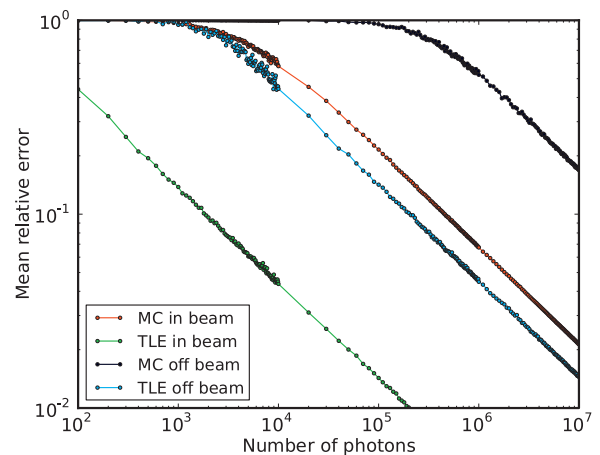


Figure 4. Comparison of the mean relative uncertainty in the ROI of the rat head, as a function of the number of incident photons for both TLE and analogous MC methods, in the slice directly irradiated and two slices away from it.

bladder and the bone areas, respectively, in the pelvis CBCT test case. The results are presented in Table 1. As anticipated, the number of deposits is much higher with the TLE method than with analogous MC (factors 54 and 21 in bladder and bone, respectively). As regards the VRF, we compared the values obtained using Eq. 12 to the ones given by Eq. 6 and 8. The difference was found to be smaller than 1%. Eq. 13 gives a rougher estimate of the VRF.

The distributions of energy deposits are plotted for the same two voxels in Fig. 5(a) and 5(c), respectively. These plots show that analogous MC deposits are much more spread than

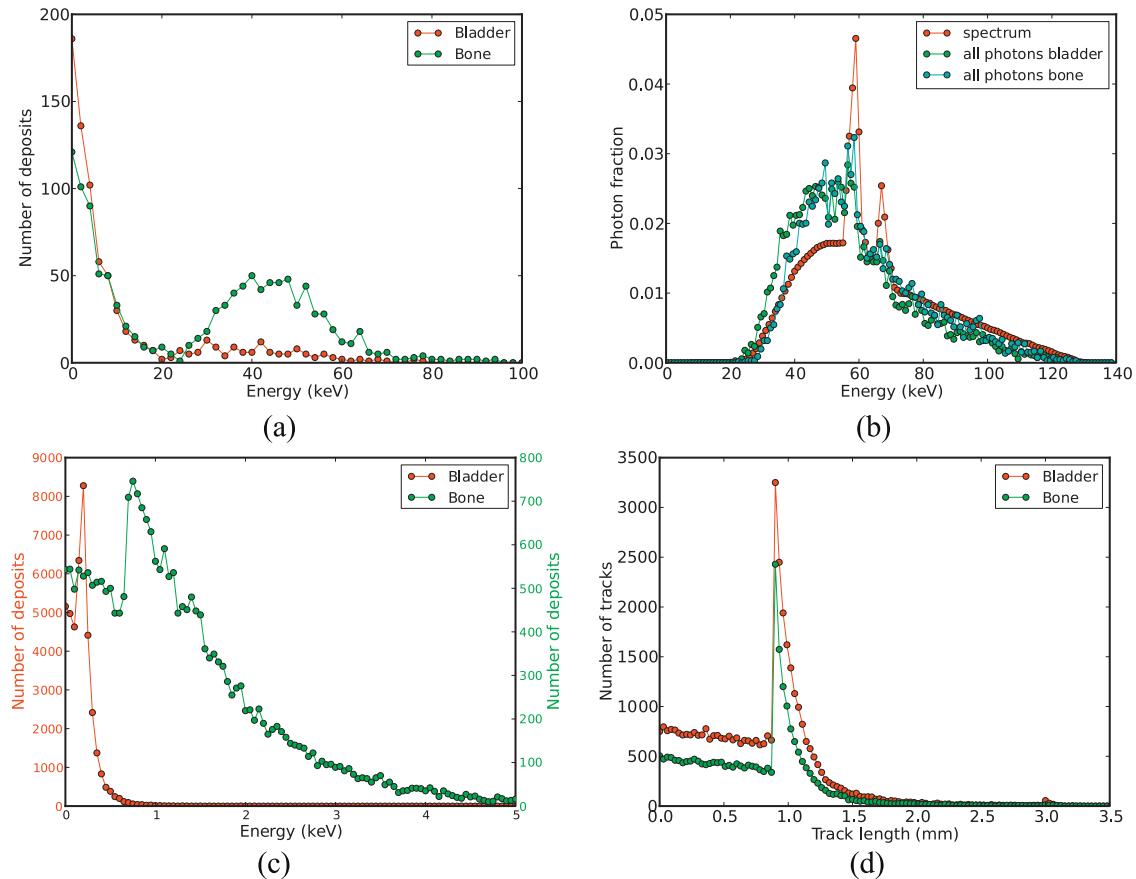


Figure 5. Analysis of the energy deposits in two voxels of the pelvis CBCT test case: (a) analogous MC energy deposits; (b) energy spectra of primary X-rays and of all X-rays falling into the bladder and bone voxels; (c) TLE energy deposits; (d) length travelled by photons in the considered voxels.

TLE deposits: e.g. for bladder, the full width at half maximum (FWHM) of the analogous MC deposits is around 5 keV while for TLE the FWHM is way below 1 keV. The shape of the energy deposits in bone in Fig. 5(a) is remarkable, with two components appearing clearly:

- an exponentially decreasing component (also present in the bladder voxel), corresponding to Compton scattering processes, with energy deposits ranging from 0 (forward-scattering) to about 20 keV (back-scattering);
- an additional component between about 20 and 70 keV; these energy deposits arise from the total photon absorption by photoelectric interactions which occur much more frequently in bone than in bladder. The shape and energy span of this component is directly related to the primary energy spectrum which is shown in Fig. 5(b), but it is softened by the attenuation coefficient (photons of lower energy values have a larger probability of interaction).

It is worthy of note in Fig. 5(b) that the overall energy spectrum of incident X-rays – for bladder and bone voxels likewise – is not hardened with respect to the primary energy

spectrum since the secondary radiation counterbalances the beam hardening.

The distribution of the lengths travelled by photons shown in Fig. 5(d) can be interpreted as follows: every position of the X-ray source around the patient corresponds to a different set of incident quasi-parallel rays crossing the relevant voxel. The highest count numbers in the histogram occur when a set of rays is orthogonal to a face of the voxel. If the rays are not exactly orthogonal to the voxel faces, the travelled length is slightly larger but the number of occurrences slightly lower. This explains the decreasing curve above the 0.908 mm discontinuity in Fig. 5(d), since in the pelvis CBCT test case the voxel size in the X-ray source plane is equal to 0.908 mm. Below the travelled length discontinuity, the number of occurrences is much lower and almost constant. Obviously, the nature of the material, here bladder or bone, does not alter this discontinuity.

The profile discontinuities of the TLE dose deposits in Fig. 5(c) come from the distribution of travelled lengths shown in Fig. 5(d). This is not straightforward, though, because the TLE energy deposit is the travelled length weighted by the incident photon energy E_{incident} (and the primary spectrum

is widely spread energetically) and by the linear energy-absorption coefficient μ_{en} (which also depends on E_{incident}). However, it appears that the product $\mu_{\text{en}}E_{\text{incident}}$ does not display large variations in the energy range of interest (Fig. 5(b)), which explains the presence of a discontinuity in the TLE energy deposit distributions of Fig. 5(c), although this discontinuity is less pronounced than in Fig. 5(d).

The distribution of energy deposits is material-dependent but the change in shape differs between analogous MC and TLE. In analogous MC, the energy deposit component related to Compton scattering processes remains in the same energy range $[0; E_{\text{Co}}^{\text{max}}]$ because $E_{\text{Co}}^{\text{max}}$ does not depend on the material; only the number of deposits may change from one material to the other. In addition, a component related to photoelectric processes may appear for materials with high atomic number elements in their composition (e.g. bone, iodine or metal implants). In TLE, the overall shape remains about the same but the distribution of energy deposits is scaled both in number of deposits and in energy between one material and the other.

3.4 Behavioural study of the variance reduction factor

Variance reduction maps are obtained by working out the ratio of the analogous and TLE MC variance estimates obtained via Eq. 6 in each voxel. The corresponding speedup factor for reaching the same statistical uncertainty is obtained taking into account the additional cost of TLE calculations (about 12% for the SSRT test case or 25% for the CBCT test case). Figure 6 shows that the VRF lies typically between 10 and 10^3 , and its value is mainly influenced by the material composition and the radiation ballistics.

As we pointed out in Sec. 2.3.3, the numerator and the denominator of Eq. 21 should be summed over the energy range of all incident photons which hit the voxel of study,

for both primary and secondary radiation. In order to get an insight into how the VRF behaves, let us assume that the dose deposited by primary radiation is prevailing, so that this sum can be restricted to it only. In the pelvis CBCT test case, the primary incident spectrum ranges from 20 to 130 keV, see Fig. 5(b). The linear attenuation and energy-absorption coefficients are given in Table 2 at two energy values in the primary spectrum (30 and 100 keV) and for two different voxels: one voxel in soft tissue (e.g. bladder) and one in bone.

Since all primary photons exhibit the same ballistics, $\langle L \rangle$ and $\sigma^2[L]$ do not depend on the incident energy and can be factorised in Eq. 21. The average traversed length being quite small in the pelvis CBCT test case ($\langle L \rangle \approx 0.77$ mm for primary radiation), the quantity $\mu_{\text{Co,Pe}} \langle L \rangle$ is much smaller than unity in the energy range of primary photons. As a result, the second term of the numerator of Eq. 21 is negligible and, using Eq. 18, one obtains:

$$\frac{\sigma^2 [\overline{D}_n, \text{analog}]}{\sigma^2 [\overline{D}_n, \text{TLE}]} \approx \frac{\langle L \rangle}{\sigma^2[L]} \frac{\sum_{\text{photons}} (\mu_{\text{Co}} \langle E_{\text{Co}}^2 \rangle + \mu_{\text{Pe}} \langle E_{\text{Pe}}^2 \rangle)}{\sum_{\text{photons}} (\mu_{\text{en}}^2 E_{\text{incident}}^2)}. \quad (22)$$

In Eq. 22, there are two contributions, related to the geometry and to the materials, respectively:

- The first contribution to the VRF $\langle L \rangle / \sigma^2[L]$ is purely geometric and is inversely proportional to the voxel size. For example, in the bladder of the pelvis CBCT, $\langle L \rangle \approx 0.77$ mm, $\sigma[L] \approx 0.45$ mm and $\langle L \rangle / \sigma^2[L] \approx 38 \text{ cm}^{-1}$, whereas in the SSRT tumour region, $\langle L \rangle \approx 0.28$ mm, $\sigma[L] \approx 0.12$ mm and $\langle L \rangle / \sigma^2[L] \approx 176 \text{ cm}^{-1}$ (numerical values given by simulations for primary radiation only). The $\langle L \rangle / \sigma^2[L]$ ratio depends strongly on the distribution of beam directions for the considered voxel. For instance, in the case of a photon

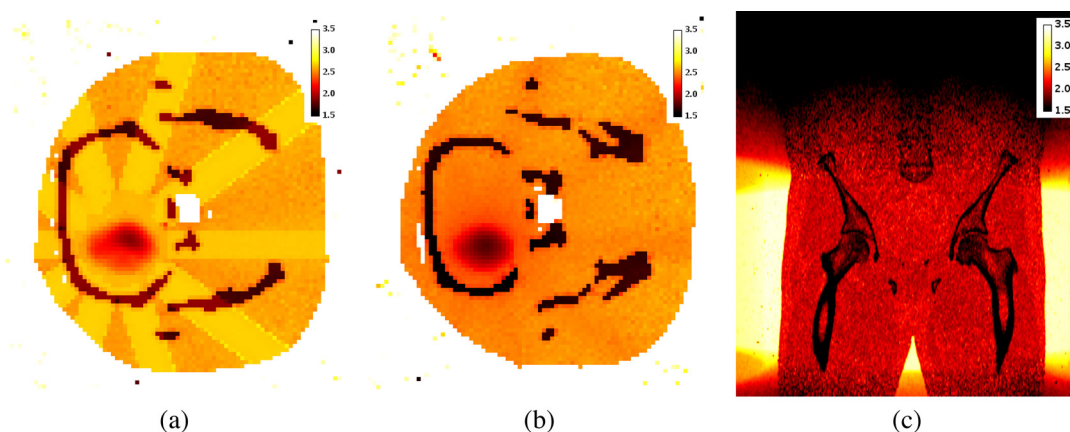


Figure 6. Maps of the analogous MC–TLE variance reduction factor. Rat head SSRT test case (10^9 incident photons): irradiated slice (a) and two slices away (b). Pelvis CBCT test case (10^8 incident photons): coronal slice (c). The colour scale is logarithmic and the powers of ten are shown in the colour bar. Note that the relative efficiency can be inferred from the VRF: it is 12% (resp. 25%) smaller, i.e. 0.05 (resp. 0.1) lower in log-scale, for the SSRT (resp. CBCT) test case.

Table 2

Linear attenuation (Compton scattering and photoelectric effect) and energy-absorption coefficients for soft tissue and cortical bone (ICRU-44).

Material	Energy (keV)	$\mu_{\text{Pe}} \text{ (cm}^{-1}\text{)}$	$\mu_{\text{Co}} \text{ (cm}^{-1}\text{)}$	$\mu_{\text{en}} \text{ (cm}^{-1}\text{)}$
Soft tissue	30	0.161	0.192	0.171
	100	0.00314	0.171	0.0270
Cortical bone	30	2.07	0.313	2.05
	100	0.0481	0.287	0.0880

beam parallel to one of the three main axes of the voxel volume, the variance $\sigma^2[L]$ of the distance travelled by the primary radiation in the voxel becomes very small. In this case, the scattered radiation becomes the predominant factor, owing to the larger randomness of its direction distribution. This is illustrated in the regions directly irradiated by the ten incident photon beams (Fig. 6(a)), in which the VRF displays values significantly higher than outside the beams.

- The second contribution is driven by the material and photon energy and is inversely proportional to the material density. This is clearly visible in Fig. 6 when comparing the variance reduction values in air, soft tissue and bone regions. Numerically, in order to estimate this contribution to the VRF in Eq. 22, we need to estimate $\langle E_{\text{Co}}^2 \rangle$ and $\langle E_{\text{Pe}}^2 \rangle$. Photons undergoing photoelectric effect deposit all their energy (the mean free path of fluorescence photons is below 0.1 mm, so that they are deemed to be locally re-absorbed). For a given E_{incident} , the variance of the photoelectric effect energy deposit is thus nought and $\langle E_{\text{Pe}}^2 \rangle = \langle E_{\text{Pe}} \rangle^2 = E_{\text{incident}}^2$. In the photon energy range of the pelvis CBCT test case, the angular distribution of Compton-scattered photons is rather isotropic over $[0, \pi]$, so that one can assume that the energy deposition follows a half-cosine distribution over the range $[0, E_{\text{Co}}^{\text{max}}]$ (maximum when radiation is π back-scattered). With the approximation that E_{Co} varies linearly against the scattering angle, the expected value of the corresponding energy deposit $\langle E_{\text{Co}} \rangle$ is then close to $E_{\text{Co}}^{\text{max}}/2$. The average energy value of the recoil electron given by the EPDL97 database is indeed close to this value in the primary energy range of the pelvis CBCT test case. From the analytical expression of the standard deviation of the half-cosine distribution [25], one finds $\langle E_{\text{Co}}^2 \rangle \approx 0.3 (E_{\text{Co}}^{\text{max}})^2$. Following calculations, the material contribution in Eq. 22 produces a factor equal to 11 cm for the soft tissue voxel and 1.8 cm for the bone voxel.

In the case of a narrow incident spectrum, the sum in Eq. 22 can be suppressed. As in most cases $\mu_{\text{Co}} \langle E_{\text{Co}}^2 \rangle \ll \mu_{\text{Pe}} \langle E_{\text{Pe}}^2 \rangle$ (below 80 keV for soft tissues and 150 keV for bone), Eq. 22 reduces simply to the ratio:

$$\frac{\sigma^2 [\overline{D}_{n, \text{ analog}}]}{\sigma^2 [D_{n, \text{ TLE}}]} \approx \frac{\langle L \rangle}{\sigma^2 [L]} \frac{\mu_{\text{Pe}}}{\mu_{\text{en}}}^2. \quad (23)$$

Although the primary spectrum of the pelvis CBCT test case is rather broad, the simplified $\mu_{\text{Pe}}/\mu_{\text{en}}^2$ ratio at 62 keV (the mean energy of the primary spectrum) is 13 cm for the soft tissue voxel and 3.5 cm for the bone voxel, which are close approximations of the more exact values given above (resp. 11 and 1.8 cm from Eq. 22). It should be noticed that the geometric and material contributions do not have the same order of magnitude: 38 cm^{-1} for the geometric contribution and between 1.8 and 11 cm for the material-related one. The VRF mostly benefits from a fine spatial sampling of the volume rather than from the tissue composition. In Fig. 6(c), the average variance reduction in the bladder region is about $120 = 10^{2.1}$ and in the bone areas about $24 = 10^{1.4}$. In both regions, the analytical estimate is about 3 to 4 times higher than the real VRF. This can be explained by the approximation of the Beer-Lambert linearization (Eq. 16) and the fact that the secondary radiation was neglected from Eq. 21 to Eq. 22.

Finally, Eq. 23 clearly emphasizes the fact that the VRF is inversely proportional to the voxel size, giving an increasing advantage to the TLE with respect to analogous MC when fine spatial resolutions are considered. This VRF behaviour translates into a corresponding efficiency gain under the assumption that the same MC engine (physical processes, navigation, scoring, etc.) is used. In addition, as regards the influence of the material composition, the second factor of the right-hand side of Eq. 23 points out that the VRF benefits from both low density and low effective atomic number.

4 Conclusion

The variance reduction provided by the TLE with respect to analogous MC originates from the large number of smaller energy deposits. A detailed statistical analysis showed how this variance reduction depends on geometric parameters (voxel size), beam parameters (ballistics and energy spectrum) and materials (density and composition). Two test cases (SSRT and CBCT) made it possible to investigate the behaviour of the TLE in clinically relevant configurations and validate our statistical modelling. The spatial distribution of the VRF was found to be very heterogeneous, with values ranging typically from 10 to 10^3 . Smaller values were found in dense regions, like bone, where more interactions take place.

The authors acknowledge the partial support of the Rhône-Alpes Research Program in hadron therapy (PRRH-Etoile), the European collaboration Envision (grant agreement no. 241851) and the DFG-Cluster of Excellence Munich-Centre for Advanced Photonics (EXE158).

References

- [1] DeMarco JJ, Wallace RE, Boedeker K. An analysis of MCNP cross-sections and tally methods for low-energy photon emitters. *Physics in Medicine and Biology* 2002;47:1321–32.
- [2] Chibani O, Williamson JF. MCPI: A sub-minute Monte Carlo dose calculation engine for prostate implants. *Medical Physics* 2005;32(12):3688–98.
- [3] van der Zee W, Hogenbirk A, van der Marck SC. ORANGE: a Monte Carlo dose engine for radiotherapy. *Physics in Medicine and Biology* 2005;50:625–41.
- [4] Taylor REP, Yegin G, Rogers DWO. Benchmarking BrachyDose. Voxel based EGSnrc Monte Carlo calculations of TG-43 dosimetry parameters. *Medical Physics* 2007;34(2):445–57.
- [5] Smans K, Zoetelief J, Verbrugge B, Haeck W, Struelens L, Vanhavere F, Bosmans H. Simulation of image detectors in radiology for determination of scatter-to-primary ratios using Monte Carlo radiation transport code MCNP/MCNPX. *Medical Physics* 2010;37(5):2082–91.
- [6] Boudou C, Balosso J, Estève F, Elleaume H. Monte Carlo dosimetry for synchrotron stereotactic radiotherapy of brain tumours. *Physics in Medicine and Biology* 2005;50:4841–51.
- [7] Edouard M, Broggio D, Prezado Y, Estève F, Elleaume H, Adam JF. Treatment plans optimization for contrast-enhanced synchrotron stereotactic radiotherapy. *Medical Physics* 2010;37(6):2445–56.
- [8] Carlsson GA. Theoretical basis for dosimetry, Vol. 1 of The dosimetry of ionizing radiation. Orlando: Academic Press; 1985. p. 1–75. Ch. 1.
- [9] Williamson JF. Monte Carlo evaluation of kerma at a point for photon transport problems. *Medical Physics* 1987;14(4):567–76.
- [10] Hubbell JH, Seltzer SM. Tables of X-ray mass attenuation coefficients and mass energy-absorption coefficients (version 1.4), [Online], available: <http://physics.nist.gov/xaamdi> [2012, January 17], National Institute of Standards and Technology, Gaithersburg, MD. (2004).
- [11] Berger MJ, Coursey JS, Zucker MA, Chang J. ESTAR, PSTAR, and ASTAR: Computer programs for calculating stopping-power and range tables for electrons, protons, and helium ions (version 1.2.3), [Online], available: <http://physics.nist.gov/Star> [2012, February 17]. National Institute of Standards and Technology, Gaithersburg, MD (2005).
- [12] Attix FH. Introduction to radiological physics and radiation dosimetry. Weinheim: Wiley-VCH; 2004. p. 607.
- [13] Freud N, Létang J, Mary C, Boudou C, Ferrero C, Elleaume H, Bravin A, Estève F, Babot D. A hybrid approach for fast simulation of dose deposition in stereotactic synchrotron radiotherapy. *IEEE Transactions on Nuclear Science* 2008;55(3):1008–17.
- [14] Cullen DE, Hubbell JH, Kissel L. EPDL97: the Evaluated Photon Data Library, '97 version, Tech. Rep. UCRL-ID-50400, Vol. 6, Rev. 5, Lawrence Livermore National Laboratory (1997).
- [15] Jan S, Santin G, Strul D, Staelens S, Assié K, Autret D, Avner S, Barbier R, Bardies M, Bloomfield P, et al. GATE: a simulation toolkit for PET and SPECT. *Physics in Medicine and Biology* 2004;49(19):4543–61.
- [16] Jan S, Benoit D, Becheva E, Carlier T, Cassol F, Descourt P, Frisson T, Grevillot L, Guigues L, Maigne L, et al. GATE V6: a major enhancement of the GATE simulation platform enabling modelling of CT and radiotherapy. *Physics in Medicine and Biology* 2011;56:881–901.
- [17] Mittone A, Baldacci F, Bravin A, Brun E, Delaire F, Ferrero C, Gasilov S, Freud N, Létang JM, Sarrut D, Smekens F, Coan P. An efficient numerical tool for dose deposition prediction applied to synchrotron medical imaging and radiation therapy. *Journal of Synchrotron Radiation* 2013;20:785–92.
- [18] Montgomery DC, Runger GC. Applied Statistics and Probability for Engineers. John Wiley & Sons; 2006.
- [19] Walters BRB, Kawrakow I, Rogers DWO. History by history statistical estimators in the BEAM code system. *Medical Physics* 2002;29(12):2745–52.
- [20] Chetty IJ, Curran B, Cygler JE, DeMarco JJ, Ezzell G, Faddegon BA, Kawrakow I, Keall PJ, Liu H, Ma C-MC, et al. Report of the AAPM Task Group No. 105: Issues associated with clinical implementation of Monte Carlo-based photon and electron external beam treatment planning. *Medical Physics* 2007;34(12):4818–53.
- [21] Ali ESM, Rogers DWO. Efficiency improvements of x-ray simulations in EGSnrc user-codes using bremsstrahlung cross-section enhancement (BCSE). *Medical Physics* 2007;34(6):2143–54.
- [22] Boone JM, Seibert A. An accurate method for computer-generating tungsten anode X-ray spectra from 30 to 140 kV. *Medical Physics* 1997;24(11):1661–70.
- [23] Schneider W, Bortfeld T, Schlegel W. Correlation between CT numbers and tissue parameters needed for Monte Carlo simulations of clinical dose distributions. *Physics in Medicine and Biology* 2000;45(2):459–78.
- [24] Smekens F, Freud N, Létang J, Adam J-F, Ferrero C, Elleaume H, Bravin A, Estève F, Babot D. Simulation of dose deposition in stereotactic synchrotron radiation therapy: a fast approach combining Monte Carlo and deterministic algorithms. *Physics in Medicine and Biology* 2009;54:4671–85.
- [25] Castrup H. Error distributions and other statistics, Tech. rep., ISG Technical Document (January 2009).

Available online at www.sciencedirect.com

ScienceDirect